NUMERICAL SIMULATION OF A SYNTHETIC JET ACTUATOR

Catalin Nae
INCAS – National Institute for Aerospace Research
Iuliu Maniu no. 220, sect. 6, 77538 Bucharest, ROMANIA
E-mail : cnae@aero.incas.ro

Keywords: *Synthetic jets, CFD, Flow control, Mesh generation*

Abstract

Synthetic jet actuator is analyzed using unsteady compressible RANS CFD code . The analysis is made for both the actuator's cavity and the surrounding domain. The actuator is considered as having a piston-like oscillatory moving bottom wall with a given amplitude and frequency. Computations are performed for the 2D case using moving grid and domain decomposition algorithms for the cavity region and the external flow. The numerical scheme used is based on explicit time marching and second order spatial accuracy. Turbulence is modeled using k-ε model with a choice of wall laws or two layer approach. Domain discretisation is based on adapted unstructured meshes using Delaunay triangularization. Several similitude parameters are used for comparison with other numerical simulations and experimental data.

Results are presented for the numerical simulation of the actuator using an imposed moving law for the bottom of the cavity. Also, influence in the surrounding field is analyzed, using apriori given velocity profile at the actuator exit.

1 Introduction

Synthetic jets (SJ) result from an oscillating diaphragm in an enclosed space, having small orifices at the top (Figure 1). They can be controlled electrostatically or using piezoelectric materials with frequencies in the range of 0.5 – 20 kHz. Because air is drawn into the cavity by the low-level suction pressure created by the diaphragm and then is expelled by the same diaphragm, such devices are considered to produce a zero-mass jet. The peak velocity and the frequency are defining parameters. For practical devices with orifice diameters like 200 μm, peak velocity may be up to 20m/s, as reported in several experiments [4][6]. Because their effect is based on a zero mass transfer, they do not need dedicated air supply systems as for other blowing/suction devices, thus making them suitable for a large class of applications.

Such actuators were previously investigated for flow control on various configurations and the results are very promising [1][6][7][9]. Several numerical studies for the actuator simulation using CFD analysis were performed in order to asses the effect of their operational characteristics [2][5]. Numerical simulation of a such device is an challenging attempt, both from theoretical point of view and in terms of computational power. Since experiment is still very difficult to imagine, CFD is until now the main analysis tool for the flow control problem using SJ actuators.

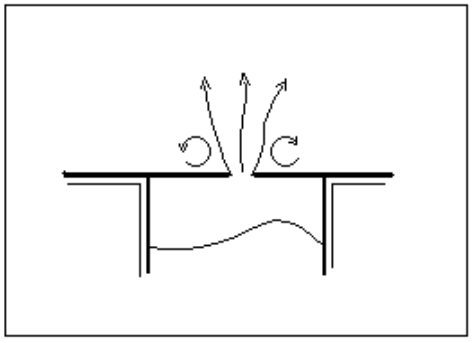

Figure 1 - Schematic of the actuator

This paper will present the numerical results and the tools used in order to investigate the flowfield generated by the actuator under several operating conditions.

2 Numerical tools

The numerical simulations in this paper are based on CFD techniques using a RANS 2D code with a modified *k-ε* turbulence model, unstructured moving meshes and domain decomposition.

2.1 The flow solver

The code used is of 2D RANS type, based on a modified *k-ε* turbulence model [3]. The code is able to use moving grids and domain decomposition. For present simulations, some modifications of the initial version were made, in order to allow a better integration of SJ specific boundary conditions.

The code is based on a combination of finite-volume and finite–element method, using general unstructured meshes and a choice of Roe or Osher schemes for the convective part of the system. The viscous part is solved using a typical centered finite element Galerkin technique. Spatial second order accuracy is obtained using a MUSCL type approach. The global formulation used by the solver is:

$$\frac{\partial}{\partial t}(W)+\nabla\cdot F(W)=\nabla\cdot N(W) \qquad (1)$$

where :

$$W=\begin{pmatrix}\rho\\ \rho\cdot U\\ \rho\cdot V\\ \rho\cdot E\\ \rho\cdot k\\ \rho\cdot\varepsilon\end{pmatrix}\quad F_x=\begin{pmatrix}\rho\cdot U\\ \rho\cdot U^2+p\\ \rho\cdot U\cdot V\\ (\rho\cdot E+p)\cdot U\\ \rho\cdot U\cdot k\\ \rho\cdot U\cdot\varepsilon\end{pmatrix}\quad F_y=\begin{pmatrix}\rho\cdot V\\ \rho\cdot U\cdot V\\ \rho\cdot V^2+p\\ (\rho\cdot E+p)\cdot V\\ \rho\cdot V\cdot k\\ \rho\cdot V\cdot\varepsilon\end{pmatrix} \qquad (2)$$

and :

$$N_x=\begin{pmatrix}0\\ \tau_{xx}\\ \tau_{xy}\\ \kappa_{tot}\frac{\partial T}{\partial x}+U\tau_{xx}+V\tau_{xy}\\ (\mu+\mu_t)\cdot\frac{\partial k}{\partial x}\\ (\mu+C_\varepsilon\cdot\mu_t)\cdot\frac{\partial\varepsilon}{\partial x}\end{pmatrix}\quad N_x=\begin{pmatrix}0\\ \tau_{xy}\\ \tau_{yy}\\ \kappa_{tot}\frac{\partial T}{\partial x}+U\tau_{xy}+V\tau_{yy}\\ (\mu+\mu_t)\cdot\frac{\partial k}{\partial y}\\ (\mu+C_\varepsilon\cdot\mu_t)\cdot\frac{\partial\varepsilon}{\partial y}\end{pmatrix} \qquad (3)$$

with :

$$\begin{aligned}&\tau_{xx}=\mu_{tot}\cdot\left(2\cdot\frac{\partial}{\partial x}U-\frac{2}{3}\cdot\nabla\cdot u\right) \qquad \nabla\cdot u=\frac{\partial}{\partial x}U+\frac{\partial}{\partial y}V\\ &\tau_{xy}=\mu_{tot}\cdot\left(\frac{\partial}{\partial y}U+\frac{\partial}{\partial x}V\right) \qquad \mu_{tot}=\mu+\mu_t\\ &\tau_{xx}=\mu_{tot}\cdot\left(2\cdot\frac{\partial}{\partial y}V-\frac{2}{3}\cdot\nabla\cdot u\right) \qquad \kappa_{tot}=\mu\cdot\frac{\gamma}{\mathrm{Pr}}+\mu_{tot}\cdot\frac{\gamma}{\mathrm{Pr}_t}\end{aligned} \qquad (4)$$

Even if the code includes a classic van Albada limiter, this feature was never used in the present calculations. The steady state solution is obtained using an iterative time marching scheme. The algorithm is either explicit in time or implicit using a GMRES and a ILU preconditioner. For unsteady flows we will use the explicit in time formulation. It was found that a four stage Runge-Kutta scheme is the best choice for the explicit solver like:

$$\frac{\partial}{\partial t}W=RHS(W) \qquad (5)$$

and :

$$\begin{aligned}&W^0=W^n\\ &W^i=W^0+\alpha_k\cdot\Delta t\cdot RHS\left(W^{i-1}\right)\mapsto i=1\ldots k\\ &W^{n+1}=W^k\end{aligned} \qquad (6)$$

where α_k coefficients have been optimized for maximum accuracy and convergence speed [3].

$$\Delta t\le\Delta t(P_i)=\min\left(\frac{\Delta x}{|u|+c},\frac{1}{2}\cdot\rho\cdot\mathrm{Pr}\cdot\frac{\Delta x^2}{\mu+\mu_t}\right) \qquad (7)$$

An important feature is the time step strategy. The general formula (7), valid for both inviscid or viscous flows, was used in order to compute the local time step at a given node . For steady state computation, a local time step strategy is commonly used. For unsteady cases, the global time step is used, as the minimum time step of all local computed time steps using the formula above. This gives up to one order of magnitude lower time step for viscous cases, so higher computational times are required [3][10].

The turbulence model used is based on the *k-ε* model. Due to the large amount of turbulent kinetic energy that is dissipated on the SJ sides edges, some important features were used in the solution approach. The grid used was designed for a $y^+ < 1$ criteria in the nozzle region. Also, a two layer formulation was used in this region,

with a fixed distance for the low Reynolds model at $y^+ = 200$. This approach was tested and compared to the use of the wall laws technique for the low local Reynolds region. For a reasonable accurate and smooth discretisation of the sensible areas, the two layer approach was considered to give better results than the classical wall laws model [7][9].

2.2 Boundary conditions

We perform two different types of simulations that have different treatment for the boundary conditions. The simulation for the external domain only is using classical treatment. In the simulation including the cavity and the external domain, cavity specific boundary conditions will be imposed. Also, for both types of simulation, because of the code formulation, we use a reference Mach number, that will be determined differently, according to the description below.

The external domain boundary conditions used are based on the characteristics method for the external flow. External flow is very sensitive to this type of conditions for the SJ simulations. For the lateral sides of the external computational domain, in order to allow the fluid to enter or leave the domain, the classical formulation was used, like :

$$\int_{S_\infty=\partial\Omega} F\cdot n\cdot d\sigma = \int_{S_\infty=\partial\Omega}\left(A^+\cdot U_{domain} + A^-\cdot U_{outside}\right)\cdot n\cdot d\sigma \qquad (8)$$

and the boundary state computed for the incoming characteristic like :

$$\begin{cases} p^* = p_{out} \\ \rho^* = \rho_i\cdot\left(\dfrac{p^*}{p_i}\right)^{1/\gamma} \\ c^{*2} = \gamma\dfrac{p^*}{\rho^*} \\ U_{boundary} = |U_i| + \dfrac{2}{\gamma-1}\left(c_i - c^*\right) \end{cases} \qquad (9)$$

However, for the top boundary of the external computational domain, this formulation has to be corrected in order to avoid reflections and to allow vortices to travel across this boundary. A modified formulation, using a pressure correction, proved to give the best results for this boundary.

$$\begin{cases} f^0 = f_0 = p^* = p_{out} \\ f^{n+1} = f_0 + \dfrac{1}{2}\left\{1-\gamma\cdot p_i\left(\dfrac{f^n}{p_i}\right)^{1/\gamma}\left[M_i + \dfrac{2}{\gamma-1}\left(1-\left(\dfrac{f^n}{p_i}\right)^{\frac{\gamma-1}{2\gamma}}\right)\right]^2\right\} \end{cases} \qquad (10)$$

The correction given by (10) is used at every point located on the upper boundary and it proved to give optimum results in only 2 cycles.

The actuator is considered to have a piston-like movement, of the sinusoidal type, with the amplitude and the frequency as defining parameters. The motion law used was the same for all points of the lower wall of the cavity domain :

$$y_{wall} = A\cdot\sin(2\pi\cdot f\cdot t) \qquad (11)$$

The amplitude is fixed and $A = d$ in all computations. This law is converted in velocity condition for the corresponding points. Pressure and density for these points are interpolated from the neighboring points inside the domain.

For the case of only external influence, the exit flow profile used was of polynomial type. The general blowing/suction law used was [2][9]:

$$v(t) = V_b(x)\sqrt{\frac{L_{ref}}{2H}}V_\infty\left[\sqrt{c_\mu} + \sqrt{\langle c_\mu\rangle}\sin\left(2\pi F^+\frac{V_\infty t}{L_{ref}}\right)\right] \qquad (12)$$

where :

$$V_b(x) = \begin{cases} V_b^0 \\ V_b^0\cdot\sin[\pi\cdot(0.5+x)] \\ V_b^0\cdot\{\sin[\pi\cdot(0.5+x)]\}^2 \end{cases} \qquad (13)$$

and global parameters given by :

$$H = \frac{1}{V_b^{0^2}}\int V_b^{\,2}(x)\cdot dx \qquad c_\mu = 2\frac{H}{L_{ref}}\left(\frac{V_b^0}{V_\infty}\right)^2$$
$$F^+ = \frac{f\cdot L_{ref}}{V_\infty} \qquad \langle c_\mu\rangle = 2\frac{H}{L_{ref}}\left(\frac{\langle v(t)\rangle}{V_\infty}\right)^2 \qquad (14)$$

In Figure 2 we present a comparison between a simple blowing/suction given by (12) and the profile resulting from the global cavity and external domain simulation at a frequency $F^+ = 5$ for the moving law.

Viscous conditions at the free external boundaries, and for the given velocity profile in the case of the external simulation, were fixed at a value of 10^{-5} for both k and ε. Solid walls and the cavity moving wall are considered as standard cases for viscous boundary conditions [3][11].

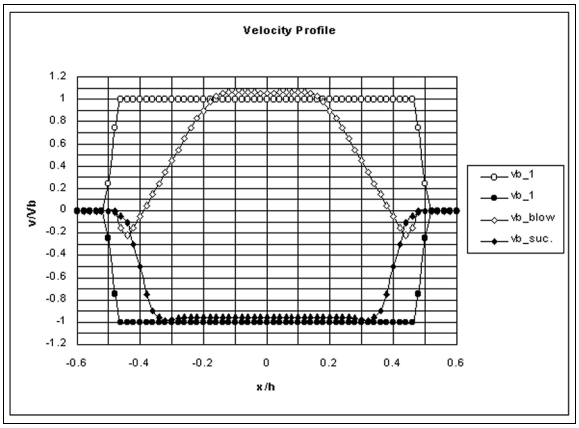

Figure 2 – SJ velocity profile

The reference Mach number was determined differently for the simulations performed. The stability requirements for the compressible code we used are as that this value has to be greater than Mach = 0.1 [3]. In the case of the cavity and external flow, because we consider the flow as induced by the moving boundary, the top speed resulting at the SJ nozzle in the blowing sequence is the reference. This is why we choose the amplitude value $A = d$, a value that gives for the exit Mach = 0.105 .We have obtained this value for A and Mach number in a two step approach from an initial guess. Also, from these global simulations, we get an estimation of the Mach number on the external lateral boundaries, in the range of Mach = 0.01. We will use this value for the case of the external simulations, and the maximum top speed for the imposed law as compared to this Mach number. This gives a ratio of 10 between the nozzle speed and the surrounding external flow on the lateral boundaries.

2.3 The mesh generator

The computational domain is partitioned in 4 distinct non-overlapping regions. For the two types of simulations, we use different grids. All data are adimensionalized by the nozzle opening d. The cavity has a fixed geometry width the nozzle length $h = 1$, and the cavity length $Lc = 15$ and width $Hc = 10$. The external domain is considered with $Lx = 30$ and $H = 50$. The computational domain has a vertical symmetry as in Figure 3.

For the global simulation, that contains 4 blocks, we use a mixed structured/unstructured triangulation. The external region, the nozzle and the main part of the cavity is using unstructured meshes. The lower part of the cavity, where we simulate the moving wall, is triangulated using a structured strip grid. This region is modified according to the motion law indicated by (11). This region is $2.1 \times A$, in order to maintain a fixed upper boundary for connectivity with the rest of the cavity domain (Figure 4). A simple algorithm is used for mesh reconstruction, at every time step, using (11), in this area during the simulation process.

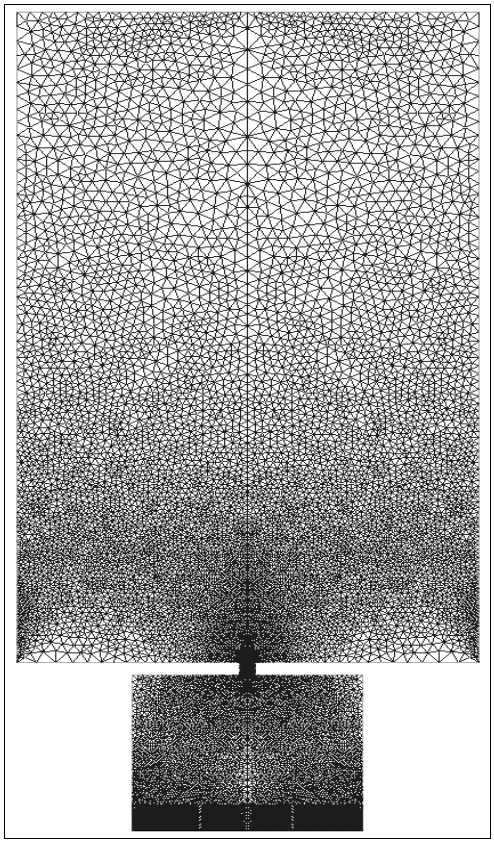

Figure 3 – Global mesh

The grid is build using standard Delaunay triangulation with imposed constraints on the

boundaries in order to achieve the required resolution around the nozzle. The imposed condition in this region was for the minimum distance to the wall in the size of 10^{-5}. This basic grid has around 25.000 points and 50.000 triangles. A number of 10 classical vertex regularizations were performed for a better shape factor distribution in the domain.

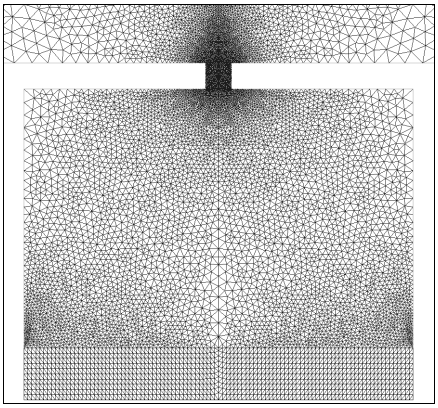

Figure 4– Cavity mesh

The external flow computations were performed using a finer grid, having the initial boundary constraints as the unstructured external initial mesh. This new mesh is strip structured, with a fine region with constant step in the central region. The number of points is 50.000 and 100.000 triangles (Figure 5).

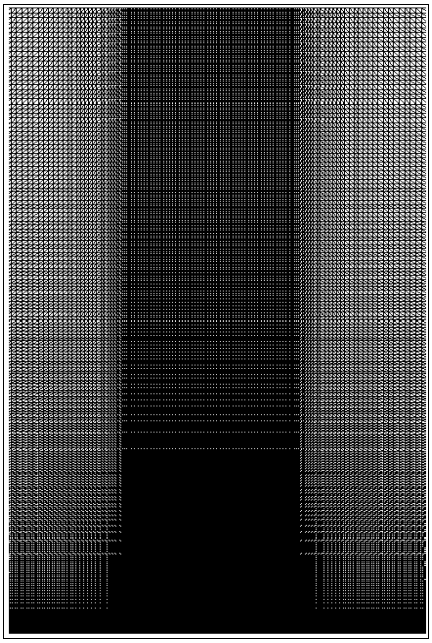

Figure 5 - Fine external mesh

Decomposition of the domain is made using non-overlapping grids, and the procedure is implemented using the points on the boundaries of the blocks and their first neighbors on every side, for the internal boundaries. A set of dummy neighbors is used for the external blocks boundaries. Decomposition of the domain was not performed in order to make use of efficient parallel computations, but to isolate the moving grid problem from the rest of the domain. This is why the moving grid region computational effort is lower than in any other regions.

3 Numerical simulations

Several types of simulations were performed in this paper. They all were intended to validate the code, boundary conditions and the meshes used. Then detailed analysis was performed for the simulation of the SJ actuator.

A special analysis was made for the validation of a reference Mach number using a given amplitude for the moving wall. The final solution used is for an amplitude of the oscillations equal to the size of the nozzle, giving a top speed Mach = 0.105 for the blowing phase. This value is a lower limit for the compressible CFD code used and is a little higher then the values currently used for SJ actuator simulations [1][8]. Velocity profiles from this simulation are presented in Figure 2. A detail of the flow in the nozzle for $F^+ = 5$ is presented in Figure 6.

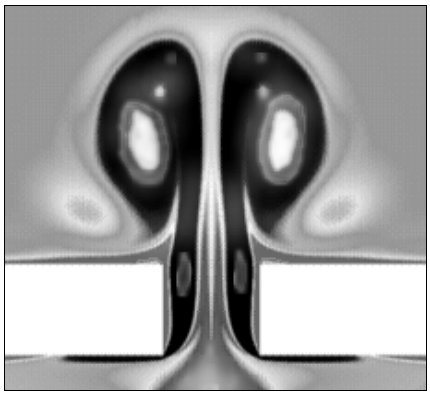

Figure 6 - Flow detail (Iso-Temperature)

The time step used in the computations is based on the global time step integration

scheme. The value is the minimum from all the local time step computed at every iteration and every point inside the domain. The lower limit of this value as 10^{-5} was used as given by (7). For the case using F+ = 5, the number of iterations for a cycle was 20.000 and up to 5 cycles were simulated, when we consider we have a converged solution inside the cavity. Cavity flow details from this simulation are presented in Figure 7.

The external flow simulations were performed using given exit laws. The most interesting case was considered the top-hat velocity profile, since from the cavity simulations it seams that this profile is valid for around 50% of the nozzle in blowing and for more than 70% in suction phase. The time step used is also global and set at 10^{-5} . Five cycles were simulated and a history of the solution was preserved for postprocessing analysis and complex visualizations. In all simulations the flow was considered turbulent at Reynolds = 1.000.

4 Results and conclusions

The first part of the simulations was intended for the analysis of the cavity flow and the shape of the velocity profile at the nozzle exit. From the converged solution as presented in Figure 2 and Figure 7 we can conclude that the main feature of the flow is the reverse profile at the extremities, present both in suction and blowing phases. Similar results have been reported by other authors [5]. This means that the active size of the SJ nozzle is smaller than the nominal value. The results prove that a simple constant velocity profile (i.e. top-hat) is valid for around 50% of the nozzle in blowing and for more than 70% in suction phase. Effects like the reverse flow for the edges of the nozzle can be neglected for outside domain, as shown from Figure 11, where there is little influence of on the decay of the centerline velocity in the external domain compared with the relevant simulation case. Also, from the global simulation of the cavity and the external flow we also conclude that the discretisation made had insufficient points in the external region for

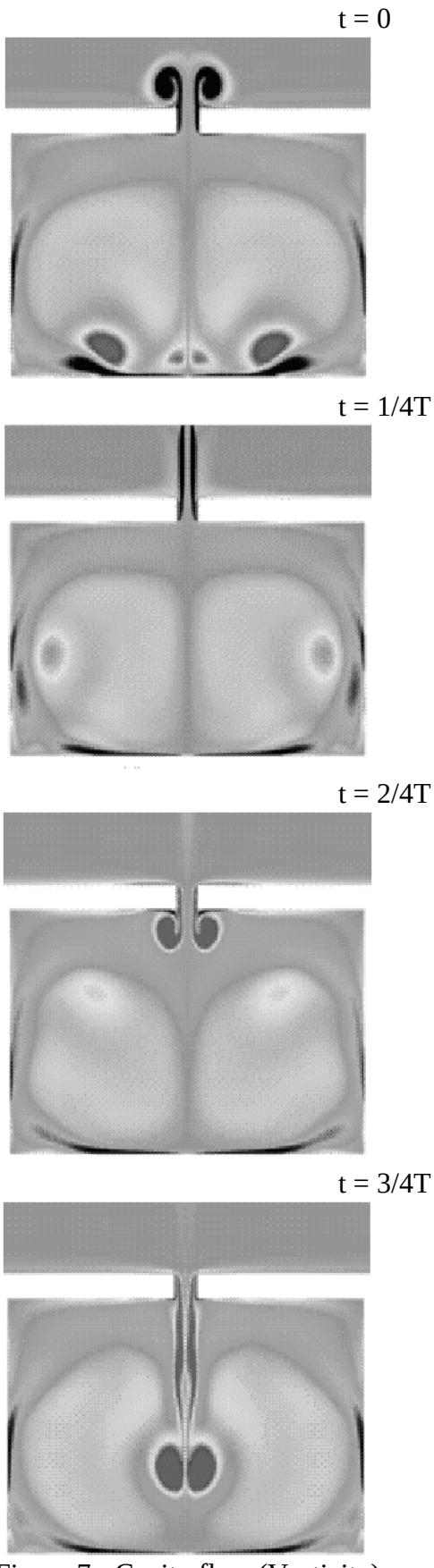

Figure 7 - Cavity flow (Vorticity)

t = 1/2T

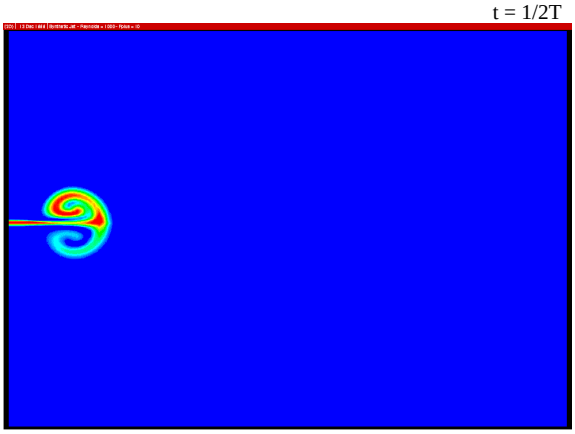

t = 3/2T

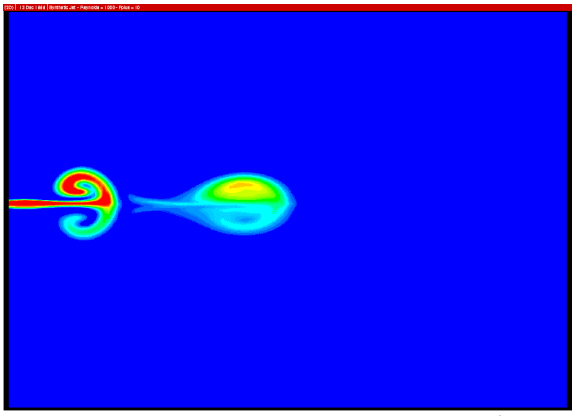

t = 5/2T

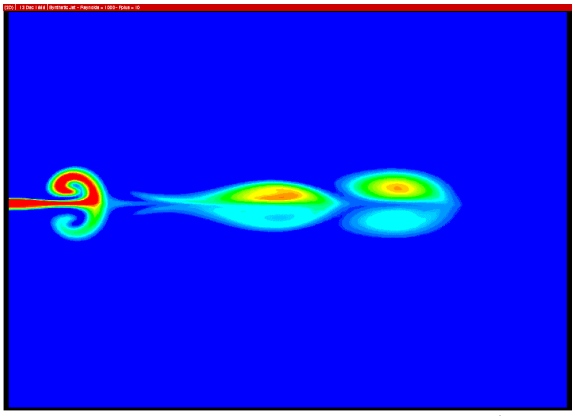

t = 7/2T

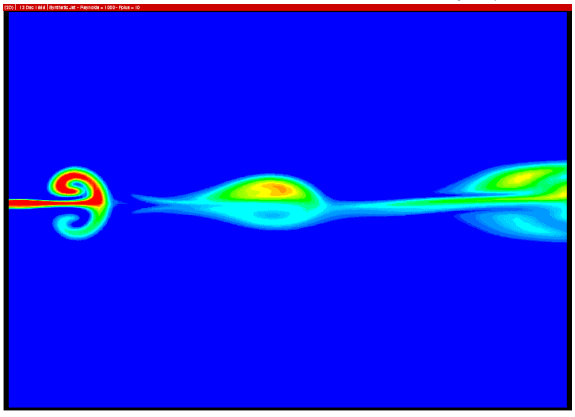

Figure 8 - External simulation F^{+}=10

t = 1/4T

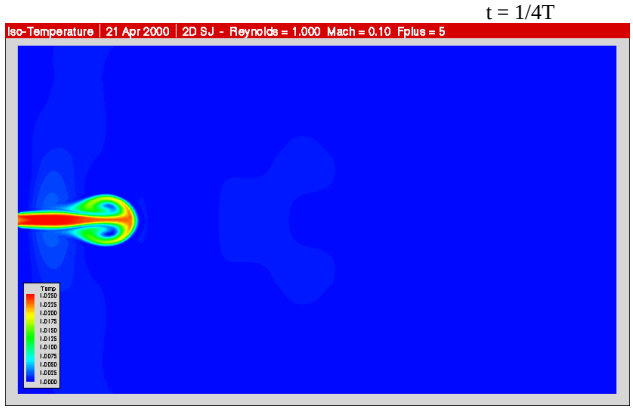

t = 1/2T

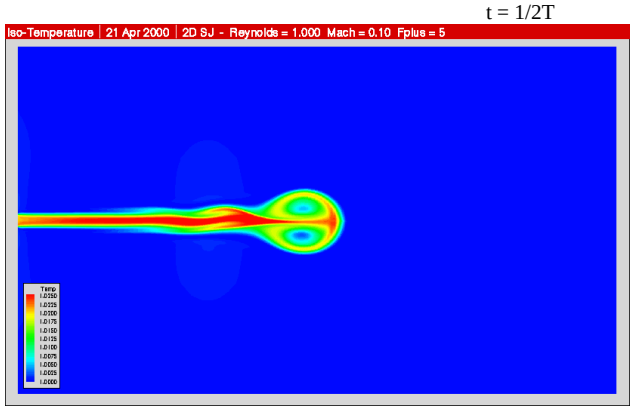

t = 3/4T

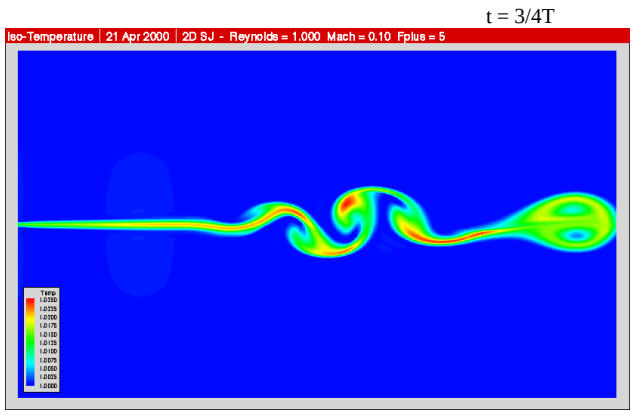

t = T

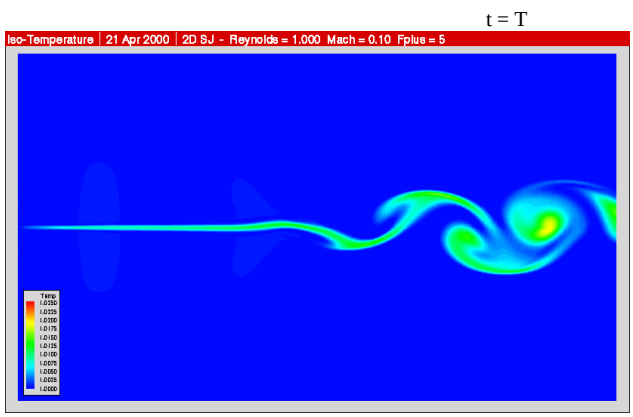

Figure 9 - External simulation F^{+}=5

the jet, but this has not affected the flow inside the cavity and the exit velocity profile.

Detailed analysis of the external flow was performed on the fine mesh using the velocity profile of the top-hat type, with the modification presented in Figure 2. Two operating frequencies were used, 5 and 10, in order to evaluate the effect of the frequency on the formation of the jet-like flow. Velocity profile was recorded at several given location and a representation of the time averaged and dimensionalized profile is presented in Figure 10. This proves that the velocity profile is almost self-similar, as indicated by other investigations [1][2][5]. For the lower frequency, the flow was found also to be unstable from a distance greater than $Hd > 10$, as presented in Figure 9. This feature is also present for the higher frequency, but with a smaller amplitude.

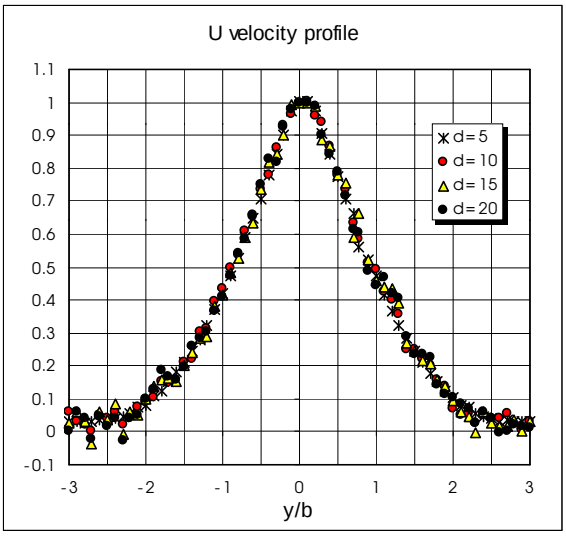

Figure 10 - Streamwise velocity profile

By comparing the decay rate of the simulations with the theoretical value of the decay for a turbulent jet, we consider that the SJ actuator is generating a jet-like flow and the decay rate is close to the theoretical value. From Figure 11 it is obvious that present simulations have a lover decay rate. This can be explained by the turbulence model used (k-ε is known to over-predict the spreading of the 2D jets [11]) and by the boundary conditions used. The ejection phenomenon seems to be overestimated by result of a rather high activity on the lateral boundaries. A solution to this problem is a larger domain, but with an increase in computational time.

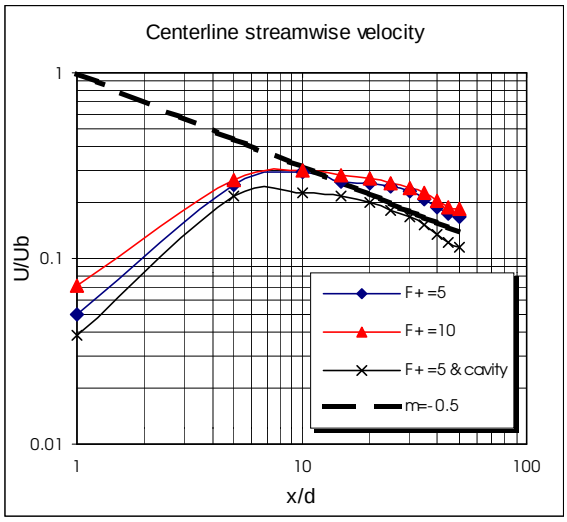

Figure 11 - Centerline velocity decay

The operating frequency of the actuator was found to have little effect on the accuracy of the velocity profile. However, the lower value for the F^+ indicated a higher instability in the external flow pattern. This behavior of the solution may also be related to the external boundary condition treatment using characteristics at very low Mach numbers. From results in Figure 8 and Figure 9 we conclude that low reflexion are present in the domain, but instability can be caused by the lateral incoming flow from external boundaries.

Another important observation is related to the difficulties of such a simulation using a compressible solver. Because of the low Mach number in the flow, convergence is very poor and some numerical problems may affect the conditions on the external boundaries. The pressure correction used was a useful cure to some instabilities problems. The experience in the present simulations will be useful in future analysis of the external pressure gradient on the velocity profile of the SJ actuator.

References

[1] Smith B L, Glezer A. *Vectoring and small-scale motions effected in free shear flows using synthetic jet actuators*. AIAA Paper 97-0213.

[2] Kral L D, Donovan J F, Cain A B, Cary A W. *Numerical simulation of synthetic jet actuators*. AIAA Paper 97-1824.

[3] Nae C. *Osher solver for unstructured grids.* INCAS report C-2070, 1998.

[4] Seifert A, Pack L G. *Oscillatory excitation of compressible flows over airfoils at flight Reynolds numbers*. AIAA Paper 99-0925.

[5] Rizzetta D P, Visbal M R, Stanek M J. *Numerical investigation of synthetic jet flowfields.* AIAA Paper 98-2910.

[6] Amitay M, Smith B L, Glezer A. *Aerodynamic flow control using synthetic jet technology.* AIAA Paper 98-0208.

[7] Nae C. *Synthetic jets influence on NACA 0012 airfoil at high angles of attack.* AIAA Paper 98-4523.

[8] Kral L D, Guo D. *Characterization of jet actuators for active flow control*. AIAA Paper 99-3573.

[9] Nae C. *Unsteady flow control using synthetic jet actuators.* AIAA Paper 2000-2403.

[10] Nae C. *Flow solver and anisotropic mesh adaptation using a change of metric based on flow variables.* AIAA Paper 2000-2250.

[11] Wilcox D C. *Turbulence modeling for CFD*. DCW Industries, 1998.